

Article

Facile One-Step Fabrication of 1T-Phase-Rich Bimetallic CoFe Co-Doped MoS₂ Nanoflower: Synergistic Engineering for Bi-Functional Water Splitting Electrocatalysis

Xinyue Li, Yahui Song ^{*}, Yiming Huang, Jihui Zhang, Siyu Wu, Wentao Zhang, Jin Wang and Xian Zhang ^{*ID}

School of Materials Science and Engineering, Qilu University of Technology, Shandong Academy of Sciences, Jinan 250353, China; lixinyue1103@163.com (X.L.); huangyiming1106@163.com (Y.H.); beckhamzjh@163.com (J.Z.); wusiyu18310202768@163.com (S.W.); 18866461235@163.com (W.Z.); wangjinsdu@qlu.edu.cn (J.W.)

^{*} Correspondence: songyahui@qlu.edu.cn (Y.S.); zhangx@qlu.edu.cn (X.Z.)

Abstract: MoS₂ has emerged as a highly promising catalyst for the hydrogen evolution reaction (HER) owing to its exceptional catalytic properties. However, there is a pressing need to further enhance its reactivity and integrate oxygen evolution reaction (OER) capabilities to facilitate its industrial implementation. In this context, a dual-metal doping approach presents a straightforward and effective strategy to achieve superior catalytic performance. Systematic characterization and electrochemical evaluations reveal that the synergistic effects of Co and Fe doping significantly enhance both HER and OER activities, demonstrating remarkable potential for practical applications in energy conversion and storage systems. The unique flower-like architecture of the material endows it with a substantially enlarged surface area, which significantly increases the exposure of active sites and facilitates enhanced catalytic activity. Specifically, it achieves the low overpotentials of -127 and 292 mV at 10 mA cm⁻² for HER and OER in alkaline media, respectively, and demonstrates excellent stability over a 10 h test. This research provides valuable insights into the development of advanced materials capable of efficiently performing both HER and OER processes, paving the way for potential applications in sustainable energy technologies.



Academic Editor: Angelo Nacchi

Received: 9 April 2025

Revised: 11 May 2025

Accepted: 22 May 2025

Published: 27 May 2025

Citation: Li, X.; Song, Y.; Huang, Y.; Zhang, J.; Wu, S.; Zhang, W.; Wang, J.; Zhang, X. Facile One-Step Fabrication of 1T-Phase-Rich Bimetallic CoFe Co-Doped MoS₂ Nanoflower: Synergistic Engineering for Bi-Functional Water Splitting Electrocatalysis. *Molecules* **2025**, *30*, 2343. <https://doi.org/10.3390/molecules30112343>

Copyright: © 2025 by the authors. Licensee MDPI, Basel, Switzerland. This article is an open access article distributed under the terms and conditions of the Creative Commons Attribution (CC BY) license (<https://creativecommons.org/licenses/by/4.0/>).

Keywords: CoFe co-doped MoS₂; synergistic effect; bifunctional; water splitting

1. Introduction

The energy scarcity and environmental deterioration caused by the overconsumption of conventional fossil fuels have forced people to search for alternative clean energy resources [1–4]. Among these, hydrogen energy has emerged as one of the most promising and ideal energy carriers, garnering significant attention [5,6]. Electrochemical water splitting offers a solution for sustainable hydrogen production through the synergistic action of the hydrogen evolution reaction (HER) and the oxygen evolution reaction (OER) [7–9]. However, due to the sluggish reaction kinetics, the development of efficient catalysts is essential to reduce reaction barriers and enhance efficiency [10,11]. Currently, noble metal-based catalysts (Pt/Ir) are widely recognized as the most advanced catalysts due to their exceptional electrocatalytic activity. However, the substantial cost and restricted reserves of these pose significant obstacles to their widespread implementation on a large scale [12–15]. Currently, most catalysts exhibit single functionality for either HER or OER, making the development of bifunctional catalysts an urgent priority [12,16–18]. Hence, the exploration

and development of low-cost high-efficiency bifunctional catalysts for electrocatalytic water splitting hold great significance.

In recent years, a diverse array of non-precious metal catalysts have been extensively investigated, encompassing transition metal sulfides [9,19–21], phosphides [22–24], oxides/hydroxides [16,25,26], nitrides [27,28], selenides [29–31], among others. Notably, transition metal chalcogenides such as MoS₂ [32–34], WS₂ [19,35], and CoS₂ [20,36] have garnered significant attention owing to their cost-effectiveness and exceptional catalytic performance. In particular, MoS₂ has been the focus of much attention due to its special two-dimensional structure, ample active sites, and notably low H⁺ adsorption Gibbs free energy, comparable to that of Pt-based catalysts [37,38]. MoS₂ exhibits three typical crystal structures: 2H, 1T, and 3R. Among them, the common 2H phase is a semiconducting phase, the 1T phase is a metallic phase, and the semiconducting 3R phase is relatively rare. The 2H phase, which exhibits thermodynamic stability, suffers from low electronic conductivity and a limited quantity of active sites, resulting in poor catalytic activity for HER [39]. On the contrary, the 1T phase has exposed catalytic active sites on both the edges and basal planes, along with enhanced electronic conductivity, making it more suitable as a catalyst for electrocatalysis [40–42]. Consequently, the development of 1T-MoS₂ holds great potential for improving the efficiency of water electrolysis.

Despite the undeniable advantages of MoS₂ in electrocatalytic HER, modifications are still necessary to lower the reaction barrier and enhance performance. Commonly used methods include elemental doping, defect engineering, constructing heterostructures, and so on. For example, Gurusamy et al. prepared a kind of co-doped MoS₂ nanoparticle as the electrode [43]. Theoretical calculations show that the ΔG_{H^*} of pure MoS₂ is 2.46 eV, indicating that it cannot bind H* strongly. However, for the co-doped MoS₂, the value of ΔG_{H^*} was found to decrease to −0.25 eV. This strongly suggests that the doping enhances the electrocatalytic activity of MoS₂ by altering its electronic structure. Significantly, its OER catalytic efficiency remains insufficient. The current research on MoS₂ predominantly focuses on improving its HER performance, with relatively few studies addressing OER enhancement [14,44,45]. However, from an industrial perspective, developing a bifunctional catalyst for HER and OER in the same electrolyte is crucial for cost-effective productivity. Element doping, particularly bimetallic element doping, stands out as a simple yet effective strategy, capable of fine-tuning the electronic structure of materials and boosting the performance of active sites [18,46–48]. Additionally, the synergistic effect of the bimetallic element components significantly plays a crucial role in modifying the electronic structure of the material, increasing the number of reaction active sites, and the optimization of the adsorption and desorption mechanisms of reaction intermediates. For instance, Muhammad Ajmal et al. synthesized an iron-doped nickel hydroxy cyanate compound, in which the doped iron atoms served as the primary active sites for catalytic activity [49]. Yajuan Pan et al. synthesized a B and Fe co-doped CoP [50]. It was shown by theoretical calculations that the energy barrier for the rate-determining step at the Fe site that was doped was rather low, signifying that the active site was truly located on the Fe site. Furthermore, Co is also a commonly employed doping element. Numerous studies have shown that doping with Co can modify the electronic structure of materials, accelerate the kinetics of water decomposition, and Co can also function as an active site for OER reactions. For example, the co-doped CuO catalyst prepared by Sieon Jung et al. reduced the potential by 180 mV compared with undoped CuO [51]. Morphological regulation of electrocatalysts is also a significant approach. To maximize the exposure of active sites to the electrolyte, it is crucial to obtain a morphology characterized by a small size and a large specific surface area [52].

In this study, we utilized a straightforward one-step hydrothermal synthesis method to develop a CoFe co-doped MoS₂ electrocatalyst with a distinctive flower-like morphology. The co-doping of Co and Fe, along with their synergistic effect, markedly enhances the HER and OER performance of the material. The unique flower-like structure provides a significantly increased specific surface area, thereby achieving the maximization of active site exposure. Importantly, the CoFe-MoS₂ catalyst exhibits superior electrochemical performance compared with both Co-MoS₂ and Fe-MoS₂, underscoring the effectiveness of bimetallic doping. In an alkaline electrolyte, CoFe-MoS₂ demonstrates exceptional catalytic performance. At a current density of 10 mA cm⁻², it achieves overpotentials of -127 mV for HER and 292 mV for OER. Moreover, it maintains excellent performance during the 10 h stability test, with only a negligible decrease in activity.

2. Results and Discussion

2.1. Structure and Morphology Characterizations

Figure 1 shows the preparation process of CoFe co-doped MoS₂. CoFe-MoS₂ was prepared by a simple one-step hydrothermal method, and in situ doping of Co and Fe was achieved by adding cobalt chloride and ferric chloride to the precursor solution. A series of MoS₂, Co-MoS₂, and Co_xFe_y-MoS₂ catalysts were prepared in order to investigate the effects of hydrochloric acid addition and heteroatom doping on MoS₂. The detailed procedures are presented in the Section 3.

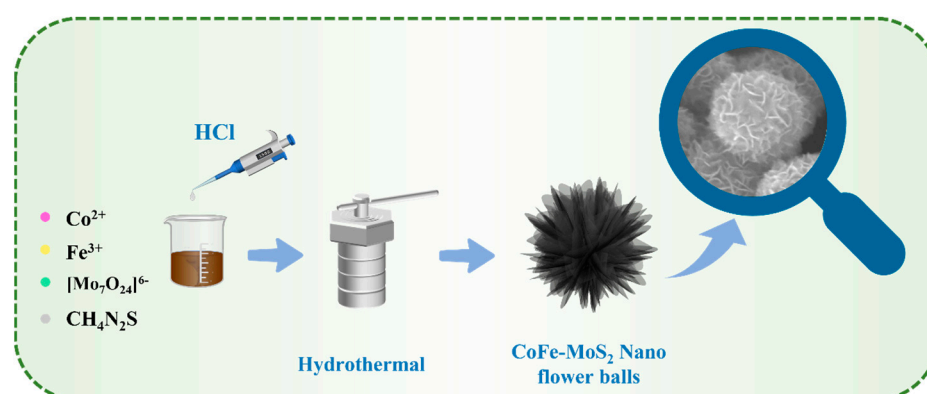


Figure 1. Schematic illustration of the synthesis procedure of CoFe-MoS₂.

The morphology of the samples was thoroughly studied by scanning electron microscope (SEM). Figures S1 and S2 show the morphologies of MoS₂ with different HCl additions. From the graph, it is clearly observed that, without the addition of HCl, the material appeared as irregular block-like shapes. When 1 mL of HCl was added, it exhibited a petal-like morphology. With the addition of 3 mL of HCl, the petal shapes were more complete and more regular. Notably, experimental optimization revealed that excessive HCl addition (5 mL) resulted in structural deformation characterized by the edge collapse of the petal-like formations. Therefore, we chose to add 3 mL of HCl as the basis for subsequent research, and added an appropriate amount of CoCl₂·6H₂O as a dopant on the basis of the original material to obtain a material with better performance. With the continuous increase in Co content, pyramid-shaped CoS₂ appeared in the SEM image, as shown in Figure S3d, indicating that the doping of Co had reached its upper limit. Through a comparison of morphology and performance, we identified 15% as the optimal doping concentration. To further enhance catalytic performance, Fe was introduced as a synergistic dopant. By adjusting the ratio of Co and Fe, we obtained the final material. From Figures 2a,b and S5, remarkably, the bimetallic doping process preserved the original petal-like architecture, yielding hierarchical flower-like microspheres with an average parti-

cle size of ~ 220 nm. These microspheres consisted of interconnected ultrathin nanosheets, creating a three-dimensional porous framework that maximized active site accessibility while maintaining structural integrity. TEM measurement was carried out to obtain more detailed information about the microstructure of the material. As shown in Figure 2c, the TEM image confirmed the hierarchical flower-like architecture, where individual petals were constructed from interconnected ultrathin nanosheets. The flower-like morphology endowed the material with a large surface area and exposed more active sites. The stacking of petals provided a multi-dimensional boundary, which is beneficial to the diffusion of electrolytes and accelerates mass transfer. In HRTEM, obvious lattice stripes of 0.278 nm and 0.631 nm were observed, corresponding to the (110) and (002) crystal planes of MoS_2 (Figure 2d,e). Elemental mapping analysis demonstrated the homogeneous dispersion of Mo, S, Co, and Fe across the three-dimensional nanoflower architecture (Figure 2f), meaning that Co and Fe elements were successfully doped into MoS_2 . The crystalline structure of the fabricated samples was subjected to further characterization by means of X-ray diffraction (XRD). The XRD patterns of the synthesized samples had the same crystal phase structure. As shown in Figure 2g, all samples exhibited identical phase structures with characteristic diffraction peaks at 13.91° , 33.02° , 39.32° , and 58.73° , respectively, corresponding to the (002), (100), (103), and (110) planes of molybdenum disulfide (JCPDS No.73-1508) [53], confirming successful MoS_2 synthesis. This shows that we successfully prepared MoS_2 . In addition, we found no obvious peak shift on the XRD pattern, which indicated that the crystal phase structure of the samples doped with Co, Fe element had not changed, and the successful doping of Co and Fe elements was achieved.

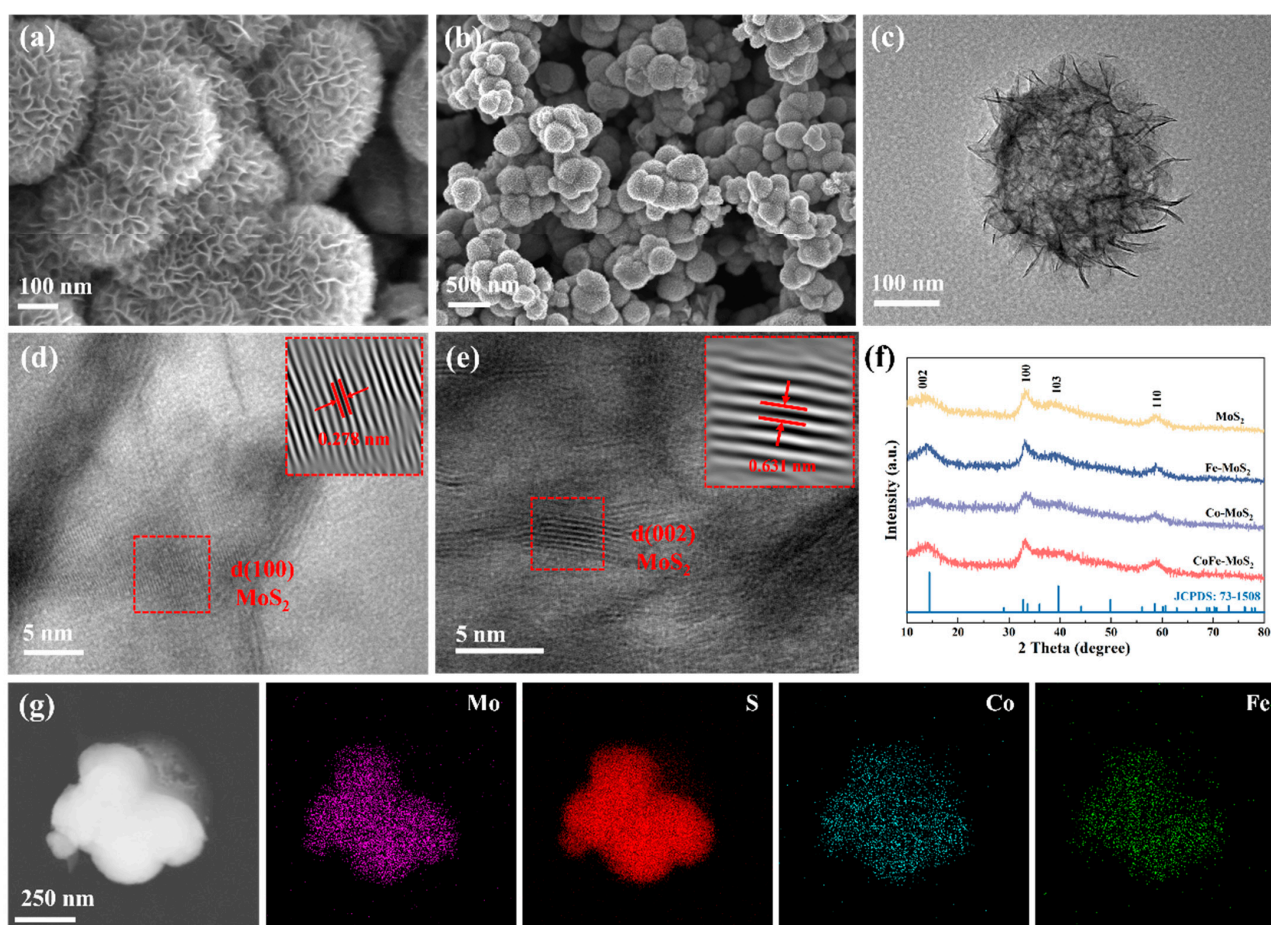


Figure 2. SEM images of (a,b) CoFe-MoS_2 . (c) TEM, (d,e) HRTEM images, (f) EDX element mapping images, and (g) XRD of CoFe-MoS_2 .

Raman analysis was conducted to further determine the particular phase composition of the synthesized CoFe-MoS₂ sample. Figure 3a shows the Raman spectra of MoS₂ and CoFe-MoS₂. Three characteristic peaks of 1T phase can be observed from the figure. The characteristic peaks of MoS₂ were located at 149.6 (J₁), 240.27 (J₂), and 337.1 (J₃) cm⁻¹, and those of CoFe-MoS₂ were located at 140.53 (J₁), 229.45 (J₂), and 329.99 (J₃) cm⁻¹, respectively [53,54]. At the same time, we also found characteristic peaks at 285.0 (E_{1g}), 379.8 (E_{12g}¹), and 406.4 (A_{1g}) cm⁻¹ of MoS₂ and 278.06 (E_{1g}), 370.9 (E_{12g}¹), and 397.5 (A_{1g}) cm⁻¹ of CoFe-MoS₂, respectively. This shows that 2H phase MoS₂ also exists in the synthesized materials. The existence of 1T phase MoS₂ improves the conductivity of the material, which is beneficial for the transmission of electrons and improves the catalytic efficiency of the material. The Raman spectra of Co-MoS₂ and Fe-MoS₂ also had similar characteristic peaks (Figures S6 and S7). Notably, the absence of significant peak shifts in the XRD patterns indicated that the crystal structure remained intact following Co and Fe doping. This structural preservation, combined with the uniform elemental distribution observed in EDS mapping, provides compelling evidence for the successful incorporation of Co and Fe dopants into the MoS₂ lattice without inducing phase transformations or structural distortions [55–57].

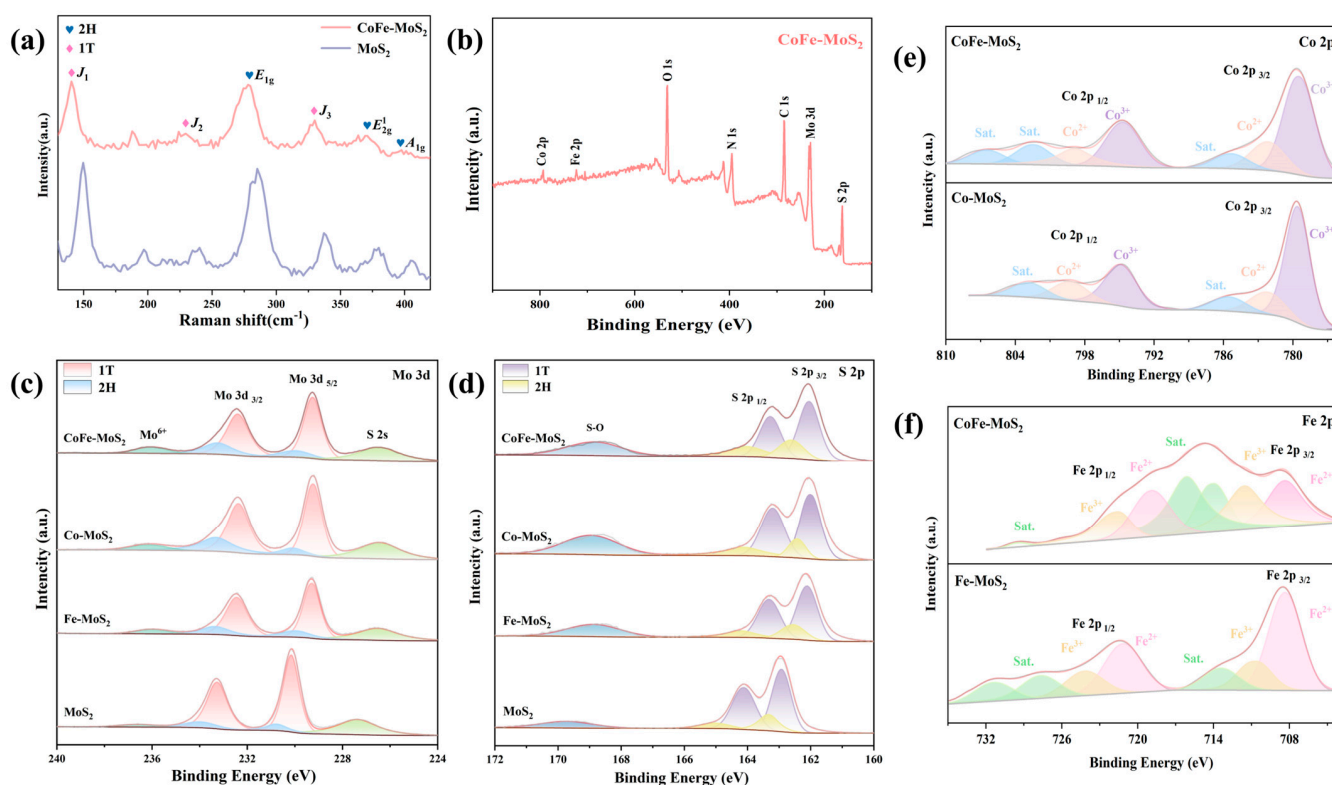


Figure 3. (a) Raman spectra, (b) overall XPS spectra of CoFe-MoS₂, (c) Mo 3d, (d) S 2p, (e) Co 2p, and (f) Fe 2p.

X-ray photoelectron spectroscopy (XPS) was utilized to probe into the surface chemical states and elemental composition of the synthesized samples. The XPS measurement spectrum in Figure 3b revealed the existence of Fe, Mo, Co, S, O, N, and C elements, which proved the successful doping of Co and Fe elements. The existence of C and N elements was derived from the reactant TAA, and the existence of O element was attributed to the inevitable oxidation of materials exposed to air. Using the C 1s peak at 284.6 eV as a reference, all spectra were calibrated. As presented in Figure 3c, the Mo 3d spectrum could be accurately fitted into six peaks. In CoFe-MoS₂, the peaks at 229.25 and 232.40 eV were attributed to Mo⁴⁺ 3d_{5/2} and Mo⁴⁺ 3d_{3/2} of 1T-MoS₂, respectively. Meanwhile, the peaks

at 229.98 and 233.24 eV referred to $\text{Mo}^{4+} 3d_{5/2}$ and $\text{Mo}^{4+} 3d_{3/2}$ of 2H- MoS_2 , proving the coexistence of 2H and 1T phases [44,54]. Additionally, the peak at 226.45 eV was assigned to S 2p, and the feature at 236.01 eV indicated the presence of Mo^{6+} species, likely resulting from surface oxidation [14]. Quantitative analysis of the Mo 3d spectra showed that the 1T phase accounted for 72.99% of the CoFe- MoS_2 sample, while the 1T phase content in MoS_2 was 66.63%, as determined by the integral area of the corresponding peaks [14,54]. This phenomenon suggests that the introduction of Co and Fe induces the generation of more 1T phases, which is conducive to the promotion of electron transport and the enhancement of the material's intrinsic conductivity. The deconvoluted S 2p spectra provided further evidence of the existence of 1T and 2H phases of CoFe- MoS_2 (Figure 3d). The peak detected at 168.85 eV could be ascribed to SO_4^{2-} species formed through surface oxidation [58]. Notably, compared with pure MoS_2 , the introduction of Co and Fe dopants induced a shift in the Mo 3d and S 2p XPS spectra of CoFe- MoS_2 , Co- MoS_2 , and Fe- MoS_2 toward lower binding energies. This phenomenon indicates that the doping of Co and Fe leads to an increase in electron cloud density, which facilitates efficient charge transfer from the Co and Fe dopants to the Mo and S sites. Consequently, the observed interaction among Co, Fe, Mo, and S demonstrates that the doping of Co and Fe efficiently regulates the electronic structure of MoS_2 , and as a result, boosts the electrocatalytic activity of the material [47,59]. Figure 3e expounded the XPS spectra of Co 2p. In CoFe- MoS_2 , it was possible to see two spin-orbit peaks, which were the $2p_{3/2}$ and $2p_{1/2}$ peaks; in addition, three shake-up satellites (referred to as Sat.) could be identified. The peaks located at 794.65 eV and 779.64 eV corresponded to the binding energies of the $\text{Co}^{3+} 2p_{1/2}$ and $2p_{3/2}$ spin orbits, respectively. The peaks at 798.39 eV and 782.23 eV were assigned to Co^{2+} , corresponding to $\text{Co}^{2+} 2p_{1/2}$ and $2p_{3/2}$, respectively [54]. The incorporation of Co into the MoS_2 lattice significantly modulated the local electronic structure, thereby activating the typically inert S atoms on the basal plane as efficient HER active sites. Figure 3f shows the Fe 2p XPS spectrum. In CoFe- MoS_2 , the peaks at 708.39 and 718.92 eV were attributed to the $2p_{3/2}$ and $2p_{1/2}$ states of Fe^{2+} , respectively. Meanwhile, the peaks at 711.57 and 721.60 eV were associated with the $2p_{3/2}$ and $2p_{1/2}$ states of Fe^{3+} [55]. Quantitative analysis of the Fe 2p spectra revealed that the Fe^{3+} content in CoFe- MoS_2 (fitted area: 875.85) was significantly higher than that in Fe- MoS_2 (fitted area: 681.55), suggesting that the introduction of Co triggers the formation of more high-valence Fe species. These high-valence Fe species are particularly advantageous for OER catalysis, as they are expected to enhance the performance of materials in OER reaction [15,55]. It is noteworthy that both Co 2p and Fe 2p of CoFe- MoS_2 exhibited a slight negative shift compared with Fe- MoS_2 and Co- MoS_2 . This phenomenon suggests that Co and Fe can interact with each other, and the synergistic effect between the two can further regulate the redistribution of electrons in the material, which in turn enhances the catalytic activity.

2.2. Electrocatalytic Performance Investigation

To make a comprehensive appraisal of the electrocatalytic performance of the synthesized materials, we employed a conventional three-electrode electrochemical system. The catalytic activities of CoFe- MoS_2 , Fe- MoS_2 , Co- MoS_2 , and MoS_2 were studied in a 1M KOH solution, with RDE supported by catalysts as the working electrode; the counter electrode was a graphite rod, and the reference electrode was an Ag/AgCl electrode, in order to reveal their performance of oxygen evolution reaction (OER) and hydrogen evolution reaction (HER).

The HER performance of the catalysts was systematically evaluated. As depicted in Figure 4a, CoFe- MoS_2 demonstrated superior catalytic activity, requiring an overpotential of only 127 mV to achieve a current density of 10 mA cm^{-2} , significantly outperforming Co-

MoS₂ (144 mV), Fe-MoS₂ (192 mV), and pristine MoS₂ (204 mV). This enhanced performance could be attributed to the synergistic effects of Co and Fe doping within the nanoflower architecture. Further optimization studies revealed that Co doping significantly improved HER activity, with 15% Co-MoS₂ exhibiting the highest performance among various doping concentrations (Figure S8). Specifically, the η_{10} values for 5% Co-MoS₂, 10% Co-MoS₂, 25% Co-MoS₂, and MoS₂ were 178 mV, 167 mV, 156 mV, and 204 mV, respectively. That is, the optimal 15% Co-MoS₂ sample attained an η_{10} value that was notably decreased. Specifically, this value was 29.4% lower than that of the MoS₂ sample. In addition, the synergistic effect of Co and Fe needed to be in the right proportion to play the best role. The LSV curves of samples with different Co and Fe ratios are shown in Figure S9. The results show that the best performance and synergistic effect exerted maximum influence when Co:Fe was 1:1. The reaction kinetics of the HER were investigated further by means of the Tafel plots. As depicted in Figure 4b, it can be observed that CoFe-MoS₂ exhibited the smallest Tafel slope (66 mV dec⁻¹), which was lower than Co-MoS₂ (73 mV dec⁻¹), Fe-MoS₂ (80 mV dec⁻¹), and MoS₂ (99 mV dec⁻¹). The observation suggests that CoFe-MoS₂ possesses greater advantages in terms of reaction kinetics [60]. Figure 4c shows that CoFe-MoS₂ had the lowest overpotential at both 10 and 50 mA cm⁻² current densities. As shown in Figure 4d, CoFe-MoS₂ displayed much lower charge transfer resistance (R_{ct}) than Co-MoS₂, Fe-MoS₂, and MoS₂, which confirms that there is faster electron transfer and more excellent HER kinetics. The R_{ct} values are in Table S1. As shown in Figure 4e and Figure S10, we utilized cyclic voltammetry to measure the electrochemical double-layer capacitances (C_{dl}) of diverse catalysts by cyclic voltammetry at different scanning rates in the non-Faraday region. Subsequently, we estimated the electrochemical surface areas (ECSA) of different catalysts based on the obtained C_{dl} values. Notably, the calculated C_{dl} values of CoFe-MoS₂, Co-MoS₂, Fe-MoS₂, and MoS₂ were 42.2, 37.8, 36.4, and 26.6 mF cm⁻², respectively. Specific ECSA values are shown in Table S2. This suggests that Co and Fe doping increases the number of active sites and CoFe-MoS₂ exposes more active sites for HER. A comprehensive performance comparison using radar charts (Figure 4f) incorporating multiple parameters (η_{10} , η_{50} , Tafel slope, C_{dl} , R_{ct}) confirmed the superior overall performance of CoFe-MoS₂. Furthermore, Figure 4g illustrates the chronoamperometry curve of CoFe-MoS₂ over 10 h. The results indicate that the current density of CoFe-MoS₂ remained at 93.7% of the initial value after 10 h. As demonstrated in Figure 4h and Table S3, the HER overpotential achieved by our CoFe-MoS₂ catalyst exhibited superior performance compared with numerous state-of-the-art electrocatalysts reported in the recent literature, showcasing its competitive advantage for practical hydrogen production applications.

Besides the HER, we also evaluated the OER performances of a range of catalysts while keeping the experimental conditions consistent. Systematic optimization revealed that the optimal OER performance was achieved at a Co doping level of 15% with a Co:Fe ratio of 1:1 (Figures S11 and S12), which was subsequently employed for further studies. Therefore, for the subsequent experiments, this Co doping level and the ratio of Co to Fe were selected. Figure 5a exhibits the linear sweep voltammetry (LSV) curves of CoFe-MoS₂, Co-MoS₂, Fe-MoS₂, and MoS₂, which indicate that CoFe-MoS₂ displayed the best OER catalytic performance compared with others. Specifically, CoFe-MoS₂ required an overpotential of only 292 mV to reach 10 mA cm⁻², significantly lower than those of Co-MoS₂ (352 mV), Fe-MoS₂ (376 mV), and pristine MoS₂. This remarkable enhancement highlights the critical importance of Co doping and the synergistic interplay between Co and Fe in boosting OER activity. Notably, undoped MoS₂ showed essentially no OER activity, further confirming the necessity of dual-metal doping. To further assess the electron-transfer kinetics of electrocatalysts, the relevant Tafel plots are shown in Figure 5b. Notably, the Tafel slope value of CoFe-MoS₂ was merely 47 mV dec⁻¹. This value was significantly much lower

than that of Co-MoS₂ (80 mV dec⁻¹), Fe-MoS₂ (62 mV dec⁻¹), and MoS₂ (226 mV dec⁻¹). This implies that CoFe-MoS₂ has faster OER kinetics under the synergistic effect of Co and Fe. Figure 5c depicts the overpotentials of different catalysts when the current densities were 10 and 50 mA cm⁻². In addition, the EIS results show the smallest charge transfer resistance (R_{ct}) of CoFe-MoS₂, much lower than that of Co-MoS₂, Fe-MoS₂, and MoS₂, indicating optimal charge transfer characteristics during OER (Figure 5d). The R_{ct} values are in Table S4. Electrochemical surface areas are a vital criterion for assessing a catalyst. To compare the catalytic activity, the electrochemical double-layer capacitance (C_{dl}) was subsequently measured (Figure 5e and Figure S13). The measured C_{dl} values were 10.3, 7.5, 4.2, and 1.3 mF cm⁻² for CoFe-MoS₂, Co-MoS₂, Fe-MoS₂, and MoS₂, respectively, implying that CoFe-MoS₂ possesses the most abundant active sites. The corresponding ECSA values are given in Table S5. As shown in the radar plot of Figure 5f, CoFe-MoS₂ exhibited the most superior OER activity when in an alkaline solution environment. Furthermore, long-term stability tests (Figure 5g) demonstrated outstanding durability, with CoFe-MoS₂ retaining 91.81% of its initial current density after 10 h of continuous operation. As evidenced in Figure 5h, the OER overpotential demonstrated by our catalyst exhibited superior performance compared with numerous state-of-the-art electrocatalysts recently reported in the literature, highlighting its competitive edge in practical water splitting systems. The corresponding specific data are given in Table S6.

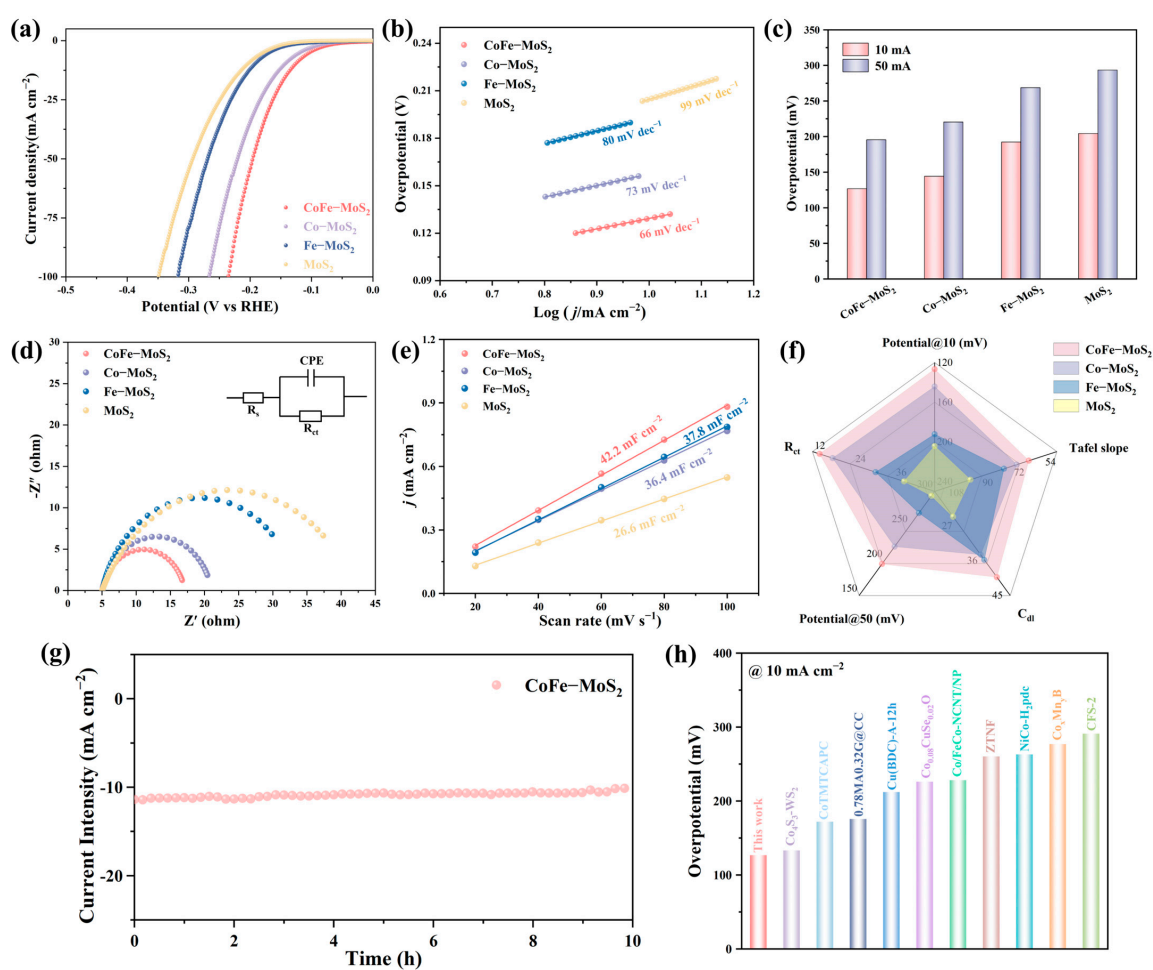


Figure 4. (a) HER polarization curve, (b) Tafel curve, (c) overpotential, (d) Nyquist plot, (e) electric double-layer capacitance of different materials. (f) Radar chart. (g) The potential versus time curve at a current density of 10 mA cm⁻². (h) Comparison of HER overpotential with the recently reported electrocatalysts from Table S3.

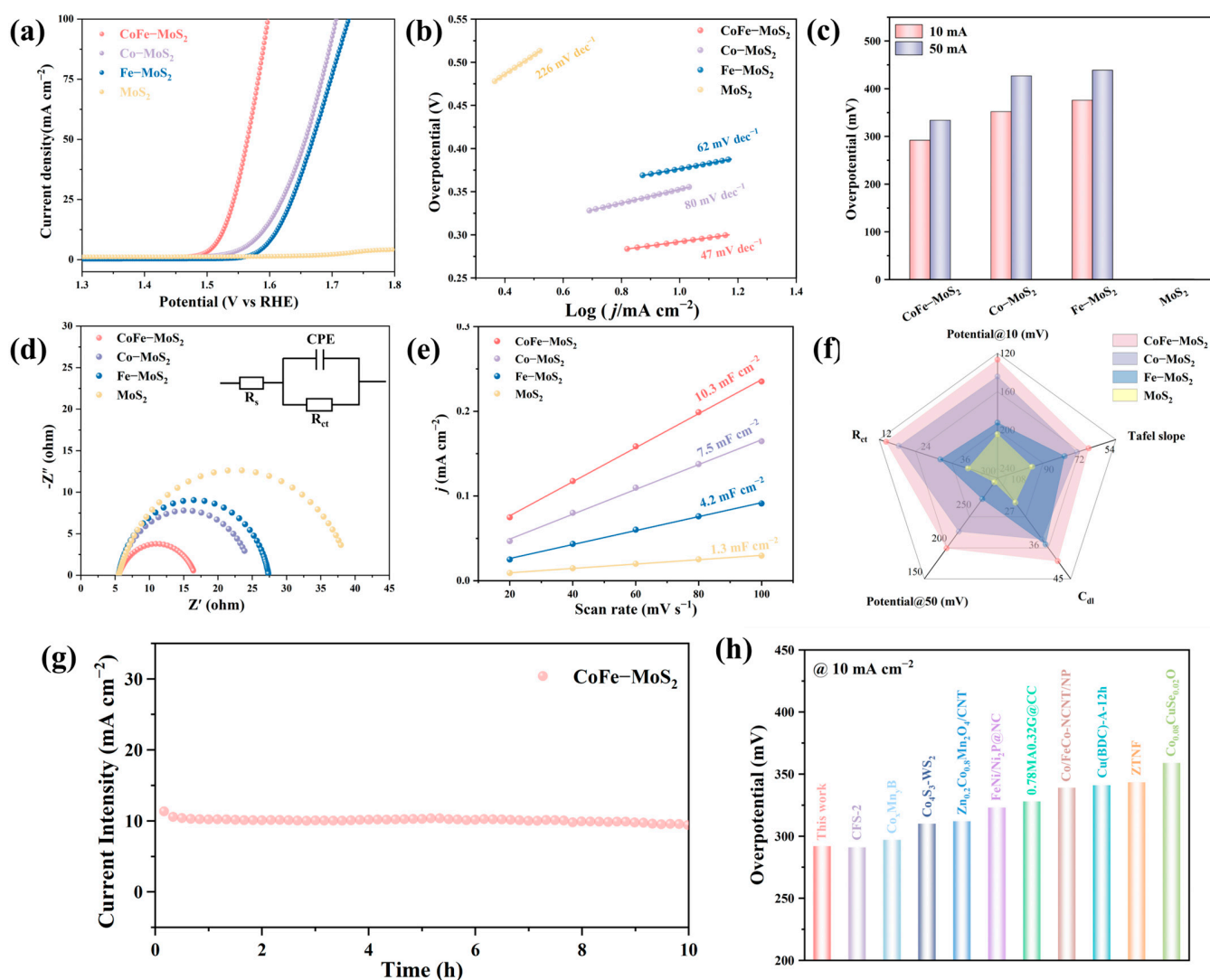


Figure 5. (a) OER polarization curve, (b) Tafel curve, (c) overpotential, (d) Nyquist plot, (e) electric double-layer capacitance of different materials. (f) Radar chart. (g) The potential versus time curve at a current density of 10 mA cm^{-2} . (h) Comparison of OER overpotential with the recently reported electrocatalysts from Table S6.

3. Materials and Methods

3.1. Materials and Reagents

All the chemicals—ammonium molybdate tetrahydrate ($(\text{NH}_4)_6\text{Mo}_7\text{O}_{24}$, Aladdin, Shanghai, China), thioacetamide (TAA, $\text{C}_2\text{H}_5\text{NS}$, Maklin, Shanghai, China), cobalt chloride hexahydrate ($\text{CoCl}_2 \cdot 6\text{H}_2\text{O}$, Aladdin, Shanghai, China), anhydrous ferric chloride (FeCl_3 , Aladdin, Shanghai, China), hydrochloric acid (HCl, 37%, Fu Yu, Tianjin, China), anhydrous ethanol (analytical grade, Sinopharm, Shanghai, China), and potassium hydroxide (KOH, Maklin, Shanghai, China)—were reagent grade and used as received without further purification. Ultrapure water was used throughout the experiments.

3.2. Synthesis of CoFe-MoS₂

CoFe-MoS₂ was synthesized via a hydrothermal treatment. Specifically, $(\text{NH}_4)_6\text{Mo}_7\text{O}_{24}$ (0.81 mmol), $\text{CoCl}_2 \cdot 6\text{H}_2\text{O}$ (0.42 mmol), and FeCl_3 (0.42 mmol) were dissolved in ultrapure water and stirred for 15 min. Subsequently, TAA (33.3 mmol) and 3 mL HCl were added, followed by an additional 15 min of stirring. Subsequently, the obtained mixture was conveyed into a 50 mL Teflon-lined stainless steel autoclave. The autoclave was then held

at a temperature of 250 °C for a duration of 24 h. Upon cooling to an ambient temperature, the black precipitate was collected by centrifugation and washed with ultrapure water and ethanol, and dried overnight at 60 °C. The final product was designated as CoFe-MoS₂.

Co-MoS₂, Fe-MoS₂, and MoS₂ were synthesized by the same method, but CoCl₂·6H₂O and FeCl₃ were removed accordingly.

3.3. Electrochemical Characterization

Electrochemical measurements were conducted using a three-electrode configuration employing the CHI 660e electrochemical workstation at an ambient temperature. A 1 M KOH solution with a pH of 14 was employed as the electrolyte. A graphite rod electrode served as the counter electrode, an Ag/AgCl electrode was used as the reference electrode, and the working electrode was a glassy carbon electrode with a diameter of 5 mm that was coated with catalyst inks.

Preparation of working electrode: A certain amount of electrocatalyst (6 mg) and XC-72 carbon powder (1 mg) was dispersed in a mixed solution containing isopropanol (480 µL) and Nafion (25 µL, 5 wt%). Then, the obtained mixture was subjected to ultrasonic treatment for 0.5 h to obtain a uniform ink. Then, 10 µL of the solution was dripped onto the glass carbon electrode (0.196 cm²), and the required working electrode (catalyst loading of 0.6 mg cm⁻²) was obtained after natural drying.

The measured potential ($E_{\text{Ag/AgCl}}$) was converted into reversible hydrogen potential (RHE) based on the following formula: $E_{\text{RHE}} = 0.198\text{V} + 0.0592 \times \text{pH} + E_{\text{Ag/AgCl}}$. HER and OER activities were evaluated on a rotating disk electrode with a rotating speed of 1600 rpm. Firstly, the glassy carbon electrode for HER and OER was measured 20 times by cyclic voltammetry at a scanning rate of 50 mV s⁻¹, and the steady-state current was obtained. Linear sweep voltammetry (LSV) was measured at a scanning rate of 5 mV s⁻¹, and 90% iR correction was performed to compensate. LSV was recorded in the range 0.2 to -0.5 V vs. RHE for HER and 1.2 to 1.8 V for OER. OER overpotential (η) was calculated by the following formula: $\eta = E_{\text{RHE}} - 1.23$. Tafel slope was obtained from LSV data by the following formula: $\eta = a \times \log |j| + b$, where “a” stands for Tafel slope, “b” stands for intercept, and “j” stands for current density. Electrochemical active surface area (ECSA) was measured by studying the electrochemical double-layer capacitance (C_{dl}) in the Faraday region. Cyclic voltammetry (CV) was carried out at different scan rates (20, 40, 60, 80, 100 mV s⁻¹) in the non-Faradaic potential range to estimate C_{dl} . By calculating the half slope (vs. RHE) of the current density difference at different scanning rates, the C_{dl} value was obtained. The equation for calculating the electrochemically active surface area (ECSA) is expressed as $\text{ECSA} = C_{\text{dl}}/C_s$. Here, C_s represents the ideal specific capacitance of the sample. In an alkaline solution, it is selected as an average value of 40 µF. Electrochemical impedance spectroscopy (EIS) was performed using a potential disturbance with an amplitude of 5 mV in the frequency range of 100,000 Hz to 0.1 Hz. To evaluate stability, chronoamperometric measurement curves were carried out at a constant current density.

3.4. Characterization

Scanning electron microscopy (SEM, Gemini, 500-70-89, Carl Zeiss, Oberkochen, Germany) and transmission electron microscopy (TEM, JEOL JEM 2100F, Tokyo, Japan) were employed to characterize the morphology and microstructure of the samples. The crystal diffraction patterns of samples were recorded by X-ray diffractometer (XRD, Smartlab SE, Rigaku, Tokyo, Japan) equipped with a Cu K α radiation source ($\lambda = 1.5418 \text{ \AA}$). The surface composition and valence state of the samples were characterized by X-ray photoelectron spectroscopy (XPS, Thermo Scientific Escalab 250Xi, Santa Clara, CA, USA). Raman

spectra (Raman) maps were obtained by an LabRAM HR Evolution Raman spectrometer (HORIBA, Villeneuve d'Ascq, France).

4. Conclusions

In summary, we successfully prepared Co and Fe co-doped flower-like MoS₂ nanostructures through a facile one-step hydrothermal method. The hierarchical flower-like architecture endows the material with a substantially enlarged specific surface area, maximizing the exposure of catalytically active sites. Notably, the material exhibits a high 1T-phase content (72.99%), which significantly enhances its electrical conductivity and facilitates rapid electron transfer during electrochemical processes. Doping the material with Co and Fe, and the resulting synergistic effect, have greatly enhanced its performance in both the HER and the OER. The optimized catalyst achieves remarkably low overpotentials of −127 and 292 mV at 10 mA cm^{−2} for HER and OER in alkaline media, coupled with robust stability over 10 h of continuous operation. This study provides a new idea for the preparation of HER and OER bifunctional catalysts with bimetallic synergistic effects and provides insights into exploring efficient catalysts for energy conversion technologies.

Supplementary Materials: The following supporting information can be downloaded at: <https://www.mdpi.com/article/10.3390/molecules30112343/s1>, Figure S1. (a,b) SEM images of the MoS₂-3mL HCl; Figure S2. SEM image of the (a,d) MoS₂-0 mL HCl, (b,e) MoS₂-1 mL HCl, and (c,f) MoS₂-5 mL HCl; Figure S3. SEM image of the Co-MoS₂ with different Co ratios (a) 5%, (b) 10%, (c) 15%, and (d) 25%; Figure S4. SEM image of the CoFe-MoS₂ with different CoFe ratios (a) Co:Fe = 1:4, (b) Co:Fe = 4:1; Figure S5. SEM image of the 15%Fe-MoS₂; Figure S6. Raman of Co-MoS₂; Figure S7. Raman of Co-MoS₂; Figure S8. HER polarization curves for the MoS₂ with different Co doping amounts; Figure S9. HER polarization curves for the MoS₂ with different Co and Fe ratios; Figure S10. C_{dil} measurements with different scanning rates of 20, 40, 60, 80, and 100 mV s^{−1} for (a) CoFe-MoS₂, (b) Co-MoS₂, (c) CoFe-MoS₂, and (d) MoS₂; Figure S11. HER polarization curves for the MoS₂ with different Co doping amounts; Figure S12. OER polarization curves for the MoS₂ with different Co and Fe ratios; Figure S13. C_{dil} measurements with different scanning rates of 20, 40, 60, 80, and 100 mV s^{−1} for (a) CoFe-MoS₂, (b) Co-MoS₂, (c) CoFe-MoS₂, and (d) MoS₂; Table S1. The R_{ct} value of different catalysts; Table S2. The ECSA value of different catalysts; Table S3. Comparison of HER performance of CoFe-MoS₂ with other electrocatalysts reported previously in 1 M KOH; Table S4. The R_{ct} value of different catalysts; Table S5. The ECSA value of different catalysts; Table S6. Comparison of OER performance of CoFe-MoS₂ with other electrocatalysts reported previously in 1 M KOH. References [61–72] are cited in Supplementary Materials

Author Contributions: Conceptualization, X.L. and Y.S.; methodology, X.L. and Y.S.; investigation, Y.H.; resources, J.W. and X.Z.; data curation, X.L.; supervision, J.Z., S.W. and W.Z.; Writing—original draft, X.L. and Y.S.; Writing—review and editing, X.L., Y.S., Y.H., J.Z., S.W., W.Z., J.W. and X.Z. All authors have read and agreed to the published version of the manuscript.

Funding: This research was funded by the Foundation (No. ZZ20200123) of State Key Laboratory of Biobased Material and Green Papermaking, Qilu University of Technology (Shandong Academy of Sciences). This work was also financially supported by the Shandong Provincial Natural Science Foundation (ZR2020QE005) and Talent Research Project (2023RCKY172) from Qilu University of Technology (Shandong Academy of Sciences).

Institutional Review Board Statement: Not applicable.

Informed Consent Statement: Not applicable.

Data Availability Statement: The data supporting this article have been included as part of the Supplementary Information.

Conflicts of Interest: The authors declare no conflicts of interest.

Abbreviations

The following abbreviations are used in this manuscript:

TAA Thioacetamide

References

1. Luo, Y.; Zhang, Z.; Chhowalla, M.; Liu, B. Recent Advances in Design of Electrocatalysts for High-Current-Density Water Splitting. *Adv. Mater.* **2022**, *34*, 2108133. [[CrossRef](#)] [[PubMed](#)]
2. Yu, Z.; Duan, Y.; Feng, X.; Yu, X.; Gao, M.; Yu, S. Clean and Affordable Hydrogen Fuel from Alkaline Water Splitting: Past, Recent Progress, and Future Prospects. *Adv. Mater.* **2021**, *33*, 2007100. [[CrossRef](#)] [[PubMed](#)]
3. Ge, B.; Deng, J.; Wang, Z.; Liang, Q.; Hu, L.; Ren, X.; Li, R.; Lin, Y.; Li, Y.; Wang, Q.; et al. Aggregate-Dominated Dilute Electrolytes with Low-Temperature-Resistant Ion-Conducting Channels for Highly Reversible Na Plating/Stripping. *Adv. Mater.* **2024**, *36*, 2408161. [[CrossRef](#)]
4. Ge, B.; Hu, L.; Yu, X.; Wang, L.; Fernandez, C.; Yang, N.; Liang, Q.; Yang, Q. Engineering Triple-Phase Interfaces around the Anode toward Practical Alkali Metal–Air Batteries. *Adv. Mater.* **2024**, *36*, 2400937. [[CrossRef](#)]
5. Wang, J.; Cui, W.; Liu, Q.; Xing, Z.; Asiri, A.M.; Sun, X. Recent Progress in Cobalt-Based Heterogeneous Catalysts for Electrochemical Water Splitting. *Adv. Mater.* **2016**, *28*, 215–230. [[CrossRef](#)]
6. Yu, Q. Boron Doping Activate Strong Metal-Support Interaction for Electrocatalytic Hydrogen Evolution Reaction in Full pH Range. *Appl. Catal. B Environ.* **2023**, *324*, 122297. [[CrossRef](#)]
7. Luyen Doan, T.L.; Nguyen, D.C.; Kang, K.; Ponnusamy, A.; Eya, H.I.; Dzade, N.Y.; Kim, C.S.; Park, C.H. Advanced Mott-Schottky Heterojunction of Semi-Conductive MoS₂ Nanoparticles/Metallic CoS₂ Nanotubes as an Efficient Multifunctional Catalyst for Urea-Water Electrolysis. *Appl. Catal. B Environ.* **2024**, *342*, 123295. [[CrossRef](#)]
8. Cheng, Y.; Zhou, X.; Pan, Q.-M.; Zhang, L.-F.; Cao, Y.-F.; Qian, T. Bimetallic Active Site Nuclear-Shell Heterostructure Enables Efficient Dual-Functional Electrocatalysis in Alkaline Media. *Rare Met.* **2023**, *42*, 3024–3033. [[CrossRef](#)]
9. Wang, Q.; Xu, H.; Qian, X.; He, G.; Chen, H. Sulfur Vacancies Engineered Self-Supported Co₃S₄ Nanoflowers as an Efficient Bifunctional Catalyst for Electrochemical Water Splitting. *Appl. Catal. B Environ.* **2023**, *322*, 122104. [[CrossRef](#)]
10. Nguyen, D.C.; Luyen Doan, T.L.; Prabhakaran, S.; Tran, D.T.; Kim, D.H.; Lee, J.H.; Kim, N.H. Hierarchical Co and Nb Dual-Doped MoS₂ Nanosheets Shelled Micro-TiO₂ Hollow Spheres as Effective Multifunctional Electrocatalysts for HER, OER, and ORR. *Nano Energy* **2021**, *82*, 105750. [[CrossRef](#)]
11. Sultan, S.; Tiwari, J.N.; Singh, A.N.; Zhumagali, S.; Ha, M.; Myung, C.W.; Thangavel, P.; Kim, K.S. Single Atoms and Clusters Based Nanomaterials for Hydrogen Evolution, Oxygen Evolution Reactions, and Full Water Splitting. *Adv. Energy Mater.* **2019**, *9*, 1900624. [[CrossRef](#)]
12. Wang, P.; Han, X.; Bai, P.; Mu, J.; Zhao, Y.; He, J.; Su, Y. Utilizing an Electron Redistribution Strategy to Inhibit the Leaching of Sulfur from CeO₂/NiCo₂S₄ Heterostructure for High-Efficiency Oxygen Evolution. *Appl. Catal. B Environ.* **2024**, *344*, 123659. [[CrossRef](#)]
13. Wei, X.; Zhang, S.; Lv, X.; Dai, S.; Wang, H.; Huang, M. Local-Reconstruction Enables Cobalt Phosphide Array with Bifunctional Hydrogen Evolution and Hydrazine Oxidation. *Appl. Catal. B Environ.* **2024**, *345*, 123661. [[CrossRef](#)]
14. Luo, Q.; Sun, L.; Zhao, Y.; Wang, C.; Xin, H.; Li, D.; Ma, F. Synergistic Effects of 1T MoS₂ and Interface Engineering on Hollow NiCoP Nanorods for Enhanced Hydrogen Evolution Activity. *J. Mater. Sci. Technol.* **2023**, *145*, 165–173. [[CrossRef](#)]
15. Wang, R.; Sun, X.; Zhong, J.; Wu, S.; Wang, Q.; (Ken) Ostrikov, K. Low-Temperature Plasma-Assisted Synthesis of Iron and Nitrogen Co-Doped CoFeP-N Nanowires for High-Efficiency Electrocatalytic Water Splitting. *Appl. Catal. B Environ. Energy* **2024**, *352*, 124027. [[CrossRef](#)]
16. Chen, J.; Li, Z.; Li, Z.; Zhou, Y.; Lai, Y. Lattice-Matched Spinel/Layered Double Hydroxide 2D/2D Heterojunction towards Large-Current-Density Overall Water Splitting. *Appl. Catal. B Environ. Energy* **2024**, *355*, 124204. [[CrossRef](#)]
17. Li, S.-M.; Liu, Z.; Li, X.-Y.; Ye, C.-F.; Li, Y.; Liu, J.-P.; Yu, S.; Sun, M.-H.; Chen, L.-H.; Su, B.-L.; et al. Synergistically Modulating D-Band Centers of Bimetallic Elements for Activating Cobalt Atoms and Promoting Water Dissociation toward Accelerating Alkaline Hydrogen Evolution. *Appl. Catal. B Environ. Energy* **2024**, *351*, 123972. [[CrossRef](#)]
18. Naresh, B.; Sreekanth, T.V.M.; Yoo, K.; Kim, J. Electrocatalytic Behavior of Transition Metal Cr and Co Doped ZnO Nanoparticles for Oxygen Evolution Reaction. *Mater. Lett.* **2024**, *373*, 137095. [[CrossRef](#)]
19. Chen, H.; Hu, M.; Jing, P.; Liu, B.; Gao, R.; Zhang, J. Constructing Heterostructure of CeO₂/WS₂ to Enhance Catalytic Activity and Stability toward Hydrogen Generation. *J. Power Sources* **2022**, *521*, 230948. [[CrossRef](#)]
20. Zeng, P.; Meng, Y.; Liu, Z.; Sun, G.; Li, X.; Yang, X.; Ye, C.; Li, Y.; Liu, J.; Chen, L.; et al. N-Doping Coupled with Co-Vacancies Activating Sulfur Atoms and Narrowing Bandgap for CoS Toward Synergistically Accelerating Hydrogen Evolution. *Small* **2023**, *19*, 2301279. [[CrossRef](#)]

21. Li, S.; Zhuo, Y.; Liu, D.; Pan, H.; Wang, Z. Anchoring Highly Surface-Exposed Pt Single Atoms on Ni₃S₂/Co₉S₈ with Abundant S Vacancies Triggers d-Orbital Electron Rearrangements for Boosted Seawater Hydrogen Evolution. *Appl. Catal. B Environ. Energy* **2024**, *355*, 124188. [[CrossRef](#)]
22. Gao, Y.; Qian, S.; Wang, H.; Yuan, W.; Fan, Y.; Cheng, N.; Xue, H.; Jiang, T.; Tian, J. Boron-Doping on the Surface Mediated Low-Valence Co Centers in Cobalt Phosphide for Improved Electrocatalytic Hydrogen Evolution. *Appl. Catal. B-Environ.* **2023**, *320*, 122014. [[CrossRef](#)]
23. Cao, W.; Zhao, R.; Liu, G.; Wu, L.; Li, J. Three-Dimensional Ordered Macroporous Design of Heterogeneous Nickel-Iron Phosphide as Bifunctional Electrocatalyst for Enhanced Overall Water Splitting. *Appl. Surf. Sci.* **2023**, *607*, 154905. [[CrossRef](#)]
24. Wang, Z.; Wang, S. Constructing Built-in Electric Field to Accelerate the Asymmetric Local Charge Distribution for Efficient Alkaline Overall Water/Seawater Splitting. *Appl. Catal. B Environ. Energy* **2024**, *352*, 124002. [[CrossRef](#)]
25. He, C.; Yang, L.; Peng, X.; Liu, S.; Wang, J.; Dong, C.; Du, D.; Li, L.; Bu, L.; Huang, X. Alkylamine-Confined Thickness-Tunable Synthesis of Co(OH)₂-CoO Nanosheets toward Oxygen Evolution Catalysis. *ACS Nano* **2023**, *17*, 5861–5870. [[CrossRef](#)]
26. Wang, B.; Chen, X.; He, Y.; Liu, Q.; Zhang, X.; Luo, Z.; Kennedy, J.V.; Li, J.; Qian, D.; Liu, J.; et al. Fe₂O₃/P-Doped CoMoO₄ Electrocatalyst Delivers Efficient Overall Water Splitting in Alkaline Media. *Appl. Catal. B Environ.* **2024**, *346*, 123741. [[CrossRef](#)]
27. Dong, Y.; Wu, A.; Yang, G.; Wang, J.; Liu, Y.; Yan, H.; Tian, C.; Fu, H. Lower-Temperature Synthesis of Nitrogen-Rich Molybdenum Nitride/Nickel (Cobalt) Heterojunctional Assembly for the Effective Water Electrolysis. *Adv. Funct. Mater.* **2024**, *35*, 2412979. [[CrossRef](#)]
28. Kavinkumar, T.; Yang, H.; Sivagurunathan, A.T.; Jeong, H.; Han, J.W.; Kim, D. Regulating Electronic Structure of Iron Nitride by Tungsten Nitride Nanosheets for Accelerated Overall Water Splitting. *Small* **2023**, *19*, 2300963. [[CrossRef](#)]
29. Qiao, H.; Li, Z.; Liu, F.; Ma, Q.; Ren, X.; Huang, Z.; Liu, H.; Deng, J.; Zhang, Y.; Liu, Y.; et al. Au Nanoparticle Modification Induces Charge-Transfer Channels to Enhance the Electrocatalytic Hydrogen Evolution Reaction of InSe Nanosheets. *ACS Appl. Mater. Interfaces* **2022**, *14*, 2908–2917. [[CrossRef](#)]
30. Zheng, H.; Wang, S.; Liu, S.; Wu, J.; Guan, J.; Li, Q.; Wang, Y.; Tao, Y.; Hu, S.; Bai, Y.; et al. The Heterointerface between Fe₁/NC and Selenides Boosts Reversible Oxygen Electrocatalysis. *Adv. Funct. Mater.* **2023**, *33*, 2300815. [[CrossRef](#)]
31. Lu, B. The CoSe₂ Hollow Cube/CoSe₂ Nanosheet Interface Catalyst for Efficient Electrolysis of Urea-Assisted Hydrogen Production at Industrial-Grade Currents. *Appl. Catal. B Environ. Energy* **2024**, *350*, 123940. [[CrossRef](#)]
32. Chen, Z.; Liu, X.; Xin, P.; Wang, H.; Wu, Y.; Gao, C.; He, Q.; Jiang, Y.; Hu, Z.; Huang, S. Interface Engineering of NiS@MoS₂ Core-Shell Microspheres as an Efficient Catalyst for Hydrogen Evolution Reaction in Both Acidic and Alkaline Medium. *J. Alloys Compd.* **2021**, *853*, 157352. [[CrossRef](#)]
33. Gonzalez-Anota, D.E.; Castaneda-Morales, E.; Paredes-Carrera, S.P.; Manzo-Robledo, A. Modulating the HER-Overpotential at the Interface of Nanostructured MoS₂ Synthesized via Hydrothermal Route: An in-Situ Mass-Spectroscopy Approach. *Int. J. Hydrogen Energy* **2023**, *48*, 17852–17867. [[CrossRef](#)]
34. Chen, D.-R.; Muthu, J.; Guo, X.-Y.; Chin, H.-T.; Lin, Y.-C.; Haider, G.; Ting, C.-C.; Kalbac, M.; Hofmann, M.; Hsieh, Y.-P. Edge-Dominated Hydrogen Evolution Reactions in Ultra-Narrow MoS₂ Nanoribbon Arrays. *J. Mater. Chem. A* **2023**, *11*, 15802–15810. [[CrossRef](#)]
35. Alsabban, M.M.; Min, S.; Hedhili, M.N.; Ming, J.; Li, L.-J.; Huang, K.-W. Growth of Layered WS₂ Electrocatalysts for Highly Efficient Hydrogen Production Reaction. *ECS J. Solid State Sci. Technol.* **2016**, *5*, Q3067–Q3071. [[CrossRef](#)]
36. Agboola, P.O.; Shakir, I.; Almutairi, Z.A.; Shar, S.S. Hydrothermal Synthesis of Cu-Doped CoS₂@NF as High Performance Binder Free Electrode Material for Supercapacitors Applications. *Ceram. Int.* **2022**, *48*, 8509–8516. [[CrossRef](#)]
37. Gao, C.; Hua, H.; Du, M.; Liu, J.; Wu, X.; Pu, Y.; Li, X. Sulfurized Co-Mo Alloy Thin Films as Efficient Electrocatalysts for Hydrogen Evolution Reaction. *Appl. Surf. Sci.* **2020**, *515*, 145842. [[CrossRef](#)]
38. Li, Z.; Xu, Y.; Ren, X.; Wang, W. Facile Synthesis of NiS₂-MoS₂ Heterostructured Nanoflowers for Enhanced Overall Water Splitting Performance. *J. Mater. Sci.* **2020**, *55*, 13892–13904. [[CrossRef](#)]
39. Zhu, D.; Liu, J.; Zhao, Y.; Zheng, Y.; Qiao, S.-Z. Engineering 2D Metal-Organic Framework/MoS₂ Interface for Enhanced Alkaline Hydrogen Evolution. *Small* **2019**, *15*, 1805511. [[CrossRef](#)]
40. Nie, K.; Qu, X.; Gao, D.; Li, B.; Yuan, Y.; Liu, Q.; Li, X.; Chong, S.; Liu, Z. Engineering Phase Stability of Semimetallic MoS₂ Monolayers for Sustainable Electrocatalytic Hydrogen Production. *ACS Appl. Mater. Interfaces* **2022**, *14*, 19847–19856. [[CrossRef](#)]
41. Bai, Z.; Wang, L.; Cao, H.; Zhang, X.; Li, G. Symbiosis of 1T and 2H Phases in the Basal Plane of Defective MoS₂ Nanoflowers for Efficient Hydrodesulfurization. *Fuel* **2022**, *322*, 124252. [[CrossRef](#)]
42. Ghanashyam, G.; Kim, H. Co-Doped 1T-MoS₂ Microspheres Embedded in N-Doped Reduced Graphene Oxide for Efficient Electrocatalysis toward Hydrogen and Oxygen Evolution Reactions. *J. Power Sources* **2024**, *596*, 234088. [[CrossRef](#)]
43. Gurusamy, P.; Perumalsamy, S.V.; Pandian, T.; Vellingiri, G.; Kulanthaivel, J.; Sinthika, S.; Mithra, K.M. Effective Solar-Driven Overall Electrocatalytic Water-Splitting by Co-Doped 1T/2H MoS₂ Nanoparticles. *Int. J. Hydrogen Energy* **2025**, *130*, 452–461. [[CrossRef](#)]

44. Kong, L.; Gao, C.; Liu, Z.; Pan, L.; Yin, P.; Lin, J. Cerium-Doped 1 T Phase Enriched MoS₂ Flower-like Nanoflakes for Boosting Hydrogen Evolution Reaction. *Chem. Eng. J.* **2024**, *479*, 147725. [[CrossRef](#)]
45. Li, B.; Nie, K.; Zhang, Y.; Yi, L.; Yuan, Y.; Chong, S.; Liu, Z.; Huang, W. Engineering Single-Layer Hollow Structure of Transition Metal Dichalcogenides with High 1T-Phase Purity for Hydrogen Evolution Reaction. *Adv. Mater.* **2023**, *35*, 2303285. [[CrossRef](#)]
46. Wu, K.; Wang, D.; Fu, Q.; Xu, T.; Xiong, Q.; Peera, S.G.; Liu, C. Co/Ce-MOF-Derived Oxygen Electrode Bifunctional Catalyst for Rechargeable Zinc–Air Batteries. *Inorg. Chem.* **2024**, *63*, 11135–11145. [[CrossRef](#)]
47. Li, H.; Du, L.; Zhang, Y.; Liu, X.; Li, S.; Yang, C.C.; Jiang, Q. A Unique Adsorption-Diffusion-Decomposition Mechanism for Hydrogen Evolution Reaction towards High-Efficiency Cr, Fe-Modified CoP Nanorod Catalyst. *Appl. Catal. B Environ.* **2024**, *346*, 123749. [[CrossRef](#)]
48. Saini, R.; Naaz, F.; El-Sheikh, M.A.; Farooq, U. Co-Doping-Assisted Systematic Evolution of a Truncated Octahedral from Tetrahedral Cu₂O for Enhanced Electrochemical OER Activity. *ACS Appl. Energy Mater.* **2024**, *7*, 8882–8893. [[CrossRef](#)]
49. Ajmal, M.; Zhang, S.; Guo, X.; Liu, X.; Shi, C.; Gao, R.; Huang, Z.-F.; Pan, L.; Zhang, X.; Zou, J.-J. Rapid Reconstruction of Nickel Iron Hydrogen Cyanamide with In-Situ Produced Proton Acceptor for Efficient Oxygen Evolution. *Appl. Catal. B Environ. Energy* **2025**, *361*, 124561. [[CrossRef](#)]
50. Pan, Y.; Wang, Z.; Wang, K.; Ye, Q.; Shen, B.; Yang, F.; Cheng, Y. Dual Doping of B and Fe Activated Lattice Oxygen Participation for Enhanced Oxygen Evolution Reaction Activity in Alkaline Freshwater and Seawater. *Adv. Funct. Mater.* **2024**, *34*, 2402264. [[CrossRef](#)]
51. Jung, S.; Senthil, R.A.; Min, A.; Kumar, A.; Moon, C.J.; Choi, M.Y. Laser-Synthesized Co-Doped CuO Electrocatalyst: Unveiling Boosted Methanol Oxidation Kinetics for Enhanced Hydrogen Production Efficiency by In Situ/Operando Raman and Theoretical Analyses. *Small Methods* **2024**, *8*, 2301628. [[CrossRef](#)]
52. Gu, Y.; Wu, A.; Jiao, Y.; Zheng, H.; Wang, X.; Xie, Y.; Wang, L.; Tian, C.; Fu, H. Two-Dimensional Porous Molybdenum Phosphide/Nitride Heterojunction Nanosheets for pH-Universal Hydrogen Evolution Reaction. *Angew. Chem.-Int. Edit.* **2021**, *60*, 6673–6681. [[CrossRef](#)]
53. Wang, J.; Sun, Z.; Li, Y.; Guo, L.; Wang, Y.; Fan, C.; Wang, Y.; Li, R.; Zhang, X.; Li, F.; et al. Sulfur Vacancy MoS₂ for Electrocatalytic Reduction of Nitrate to Ammonia with Enhanced Selectivity. *J. Alloys Compd.* **2023**, *955*, 170199. [[CrossRef](#)]
54. Liu, H.; Zhang, S.; Chai, Y.; Dong, B. Ligand Modulation of Active Sites to Promote Cobalt-Doped 1T-MoS₂ Electrocatalytic Hydrogen Evolution in Alkaline Media. *Angew. Chem. Int. Edition* **2023**, *62*, e202313845. [[CrossRef](#)]
55. Dong, J.; An, B.; Liu, W.; Su, H.; Li, N.; Gao, Y.; Ge, L. Cation-Induced Interface Electric Field Redistribution and Molecular Orbital Coupling in Co-FeS/MoS₂ for Boosting Electrocatalytic Overall Water Splitting. *Chem. Eng. J.* **2024**, *498*, 155102. [[CrossRef](#)]
56. Sang, Y.; Xue, J.; Hu, J.; Chen, L. High-Current Density Alkaline Water/Seawater Splitting by Mo and Fe Co-Doped Ni₃S₂: Invariant Active Sites with Accelerated Water Dissociation Kinetics. *Appl. Catal. B Environ. Energy* **2025**, *361*, 124698. [[CrossRef](#)]
57. Xu, X.; Guo, K.; Sun, J.; Yu, X.; Miao, X.; Lu, W.; Jiao, L. Interface Engineering of Mo-doped Ni₂P/Fe_xP-V Multiheterostructure for Efficient Dual-pH Hydrogen Evolution and Overall Water Splitting. *Adv. Funct. Mater.* **2024**, *34*, 2400397. [[CrossRef](#)]
58. Cheng, X.; Tong, Y. Interface Coupling of Cobalt Hydroxide/Molybdenum Disulfide Heterostructured Nanosheet Arrays for Highly Efficient Hydrazine-Assisted Hydrogen Generation. *ACS Sustain. Chem. Eng.* **2023**, *11*, 3219–3227. [[CrossRef](#)]
59. Sun, L.; Zhou, Z.; Xie, Y.; Zheng, J.; Pan, X.; Li, L.; Zhao, G. Surface Self-Reconstruction of Fe-Ni₃S₂ Electrocatalyst for Value-Generating Nitrile Evolution Reaction to Drive Efficient Hydrogen Production. *Adv. Funct. Mater.* **2023**, *33*, 2301884. [[CrossRef](#)]
60. Deng, Y.; Cao, Y.; Xia, Y.; Xi, X.; Wang, Y.; Jiang, W.; Yang, D.; Dong, A.; Li, T. Self-Templated Synthesis of CoFeP@C Cage-In-Cage Superlattices for Enhanced Electrocatalytic Water Splitting. *Adv. Energy Mater.* **2022**, *12*, 2202394. [[CrossRef](#)]
61. Wang, J.; Ling, Q.; Yao, Y.; Zhu, D.; Shu, S.; Zhou, Z.; Wu, X.; Wu, P. Willow Catkin-like Co₄S₃-WS₂ Nanostructured Electrocatalyst for Efficient Overall Alkaline Water Splitting. *ACS Appl. Nano Mater.* **2024**, *7*, 24408–24416. [[CrossRef](#)]
62. Mounesh; Thippeswamy, B.A.; Shiralkar, P.; Balakrishna, R.G.; Nagaraja, B.M.; Pramoda, K. Non-Precious Tetra-(4-Methylthiazole)-Carboxamide Cobalt(II) Phthalocyanine Supported on Functionalized Carbon Nanotubes as an Efficient Electrocatalyst for a Hydrogen Evolution Reaction. *ACS Appl. Energy Mater.* **2024**, *8*, acaem.4c01292. [[CrossRef](#)]
63. Cheng, T.; Chen, C.; Wen, M.; Pan, F.; Zhang, X.; Ma, H.; Hou, B.; Xin, X. Low-Cost Composite Electrodes by Active Fe₃O₄ (111) of Fly Ash Magnetic-Sphere for Efficient Electrochemical Overall Water Splitting. *Int. J. Environ. Sci. Technol.* **2025**, *24*, 1475–1496. [[CrossRef](#)]
64. Shoostari Gugtapeh, H.; Abbasi, M.; Hasanzadeh Moghadam, M.; Rezaei, M. Solvent-Exchange-Assisted Activation of Cu-1,4-Benzene Dicarboxylate Metal-Organic Framework for Use as a Bifunctional Water Splitting Electrocatalyst. *Electrochim. Acta* **2024**, *508*, 145224. [[CrossRef](#)]
65. Rashid, U.; Zhu, Y.; Cao, C. Microwave Assisted Synthesis of Cobalt-Doped Copper Selenite Nanorice as Bifunctional Electrocatalyst for Overall Water Splitting. *J. Electroanal. Chem.* **2024**, *962*, 118267. [[CrossRef](#)]
66. Zhang, Y.; Liu, X.; Wan, Z.; Wang, Z.; Gao, F.; Xuan, C. Nitrogen-Doped Carbon Nanotubes/Nanoparticles Confined Co/FeCo Composites with Metal-Nitrogen Sites for Efficient Multifunctional Electrocatalysis. *J. Environ. Chem. Eng.* **2024**, *12*, 114326. [[CrossRef](#)]

67. Huang, C.; Zhan, G.; Xiao, Z.; Lin, S. Synergistic Dual-Functional Full Deionization and Electrocatalysis of Water by ZnO/Ti₃C₂T_x Heterojunction Supported with Novel Template. *Next Mater.* **2024**, *5*, 100267. [[CrossRef](#)]
68. Zahid, R.; Abdul Karim, M.R.; Khan, F.S.; Zeb, G.; Marwat, M.A.; Khan, M.Z.; Gohar, O.; Haq, E.U. Catalytically Active Bimetallic Nickel–Cobalt MOF Linked Via Pyridine 2, 6-Dicarboxylate for Electrochemical Water Splitting Applications. *Arab. J. Sci. Eng.* **2025**, *50*, 6625–6637. [[CrossRef](#)]
69. Li, S.; Wang, Z.; Yang, Y.; Pan, S.; Pan, W.; Tang, M.; Liu, K. Electronic Modulation of MOF-Derived Co_xMn_yB Nanosheet Arrays toward Efficient Bifunctional Electrocatalysts for Water Splitting. *J. Electroanal. Chem.* **2024**, *970*, 118553. [[CrossRef](#)]
70. Han, Z.; Zhang, Y.; Lv, T.; Tan, X.; Wang, Q.; Wang, Y.; Meng, C. Core-Shell Cobalt-Iron Silicide Electrocatalysts with Enhanced Bifunctional Performance in Hydrogen and Oxygen Evolution Reactions. *J. Colloid Interface Sci.* **2025**, *682*, 1–10. [[CrossRef](#)]
71. Kang, H.; Liu, Y.; Wei, M.; Zhou, L.; Wang, C. Activating Spinel CoMn₂O₄ Supported on CNT via Zn Substitution for Bifunctional Oxygen Electrocatalysis. *J. Alloys Compd.* **2024**, *1000*, 175089. [[CrossRef](#)]
72. Yu, T. FeNi/Ni₂P Nanoparticles Encapsulated in Nitrogen-Doped Porous Carbon: Efficient Electrocatalysts for Oxygen Evolution Reaction. *J. Mater. Sci.* **2024**, *59*, 21710. [[CrossRef](#)]

Disclaimer/Publisher’s Note: The statements, opinions and data contained in all publications are solely those of the individual author(s) and contributor(s) and not of MDPI and/or the editor(s). MDPI and/or the editor(s) disclaim responsibility for any injury to people or property resulting from any ideas, methods, instructions or products referred to in the content.